7-2019

Scaling of an atmospheric model to simulate turbulence and cloud microphysics in the Pi Chamber

Subin Thomas
Michigan Technological University, subint@mtu.edu

Mikhail Ovichinnikov
Pacific Northwest National Laboratory

Fan Yang
Brookhaven National Laboratory

Dennis van der Voort
Michigan Technological University

Will Cantrell
Michigan Technological University, cantrell@mtu.edu

See next page for additional authors

Recommended Citation

Thomas, S., Ovichinnikov, M., Yang, F., van der Voort, D., Cantrell, W., Krueger, S. K., & Shaw, R. (2019). Scaling of an atmospheric model to simulate turbulence and cloud microphysics in the Pi Chamber. *Journal of Advances in Modeling Earth Systems, 11*, 1981-1994. http://dx.doi.org/10.1029/2019MS001670

Retrieved from: https://digitalcommons.mtu.edu/michigantech-p/639

Follow this and additional works at: https://digitalcommons.mtu.edu/michigantech-p

 Part of the Physics Commons

JAMES | Journal of Advances in Modeling Earth Systems

RESEARCH ARTICLE
10.1029/2019MS001670

Scaling of an Atmospheric Model to Simulate Turbulence and Cloud Microphysics in the Pi Chamber

Subin Thomas[1], Mikhail Ovchinnikov[2], Fan Yang[3], Dennis van der Voort[1], Will Cantrell[1], Steven K. Krueger[4], and Raymond A. Shaw[1]

[1]Michigan Technological University, Houghton, MI, USA, [2]Pacific Northwest National Laboratory, Richland, WA, USA, [3]Brookhaven National Laboratory, Upton, NY, USA, [4]University of Utah, Salt Lake City, UT, USA

Key Points:
- A large-eddy simulation with spectral bin cloud microphysics is scaled to simulate a laboratory convection chamber
- The simulated mixing state and turbulence properties reasonably compare with a simple flux model and with measurements
- The simulation replicates published observations from the Pi Chamber, including steady-state clouds and size distribution broadening.

Supporting Information:
- Supporting Information S1

Correspondence to:
R. A. Shaw,
rashaw@mtu.edu

Citation:
Thomas, S., Ovchinnikov, M., Yang, F.,van der Voort, D., Cantrell, W., Krueger, S. K., & Shaw, R. A. (2019).Scaling of an atmospheric model to simulate turbulence and cloud microphysics in the Pi Chamber. *Journal of Advances in Modeling Earth Systems*, *11*, 1981–1994. https://doi.org/10.1029/2019MS001670

Received 22 FEB 2019
Accepted 23 MAY 2019
Accepted article online 29 MAY 2019
Published online 2 JUL 2019

Abstract The Pi Cloud Chamber offers a unique opportunity to study aerosol-cloud microphysics interactions in a steady-state, turbulent environment. In this work, an atmospheric large-eddy simulation (LES) model with spectral bin microphysics is scaled down to simulate these interactions, allowing comparison with experimental results. A simple scalar flux budget model is developed and used to explore the effect of sidewalls on the bulk mixing temperature, water vapor mixing ratio, and supersaturation. The scaled simulation and the simple scalar flux budget model produce comparable bulk mixing scalar values. The LES dynamics results are compared with particle image velocimetry measurements of turbulent kinetic energy, energy dissipation rates, and large-scale oscillation frequencies from the cloud chamber. These simulated results match quantitatively to experimental results. Finally, with the bin microphysics included the LES is able to simulate steady-state cloud conditions and broadening of the cloud droplet size distributions with decreasing droplet number concentration, as observed in the experiments. The results further suggest that collision-coalescence does not contribute significantly to this broadening. This opens a path for further detailed intercomparison of laboratory and simulation results for model validation and exploration of specific physical processes.

1. Introduction

Large-eddy simulation (LES) has been used for studies of clouds since the 1970s and 80s (Deardorff, 1980; Moeng, 1986), with the sophistication of cloud microphysics representation progressing steadily (e.g., Kogan et al., 1995; Khairoutdinov & Kogan, 2000; Stevens et al., 1998). LES has since been used in studying a wide range of cloud problems: from aerosol indirect effects (Xue & Feingold, 2006), to deep tropical convection (Khairoutdinov et al., 2009), to Arctic mixed-phase clouds (Ovchinnikov et al., 2014). Validation has typically been accomplished through model intercomparisons (e.g., Ovchinnikov et al., 2014; Siebesma et al., 2003) and carefully designed field projects (e.g., Khairoutdinov & Kogan, 1999; Neggers et al., 2003; Stevens et al., 2005). For detailed cloud studies, aerosols and clouds represented through "bin microphysics" (e.g., Khain et al., 2000) are often considered the gold standard, but recently, it has been recognized that numerical artifacts can become dominant (Morrison et al., 2018). This surprising result emphasizes yet again the critical importance of rigorous model evaluation against the best possible measurements (Wyngaard, 1998a).

The purpose of this paper is to explore the ability of a widely used LES model with detailed (spectral bin) cloud microphysics, to capture the observed behavior of convection and cloud properties in a laboratory convective-cloud chamber. The Pi Cloud Chamber (Chang et al., 2016) generates clouds through isobaric mixing in turbulent Rayleigh-Bénard convection. Because aerosol input and thermodynamic forcing are independently and externally controlled, it offers a unique opportunity to explore turbulence-microphysics interactions (Chandrakar et al., 2016, 2017; Desai et al., 2018). Besides the well-characterized boundary and input conditions, turbulence and microphysical properties can be sustained in a dynamic steady state, with aerosol injection and cloud droplet activation balanced by droplet growth and sedimentation. This facilitates comparison to the LES cloud model and provides an opportunity to evaluate its ability to simulate the observed dynamics and microphysical processes in the cloud chamber. The interaction is two way, because the model can also be powerful in helping to interpret measurements and providing guidance for future experiments.

The idealized Rayleigh-Bénard theory does not include sidewalls; following convention in the fluid mechanics literature (Chillà & Schumacher, 2012), however, we will continue to refer to turbulent convection in an

enclosed chamber as Rayleigh-Bénard convection. The Pi Cloud Chamber, if constructed according to the typical confined Rayleigh Bénard model, would have unstable temperature gradient along the direction of gravity and adiabatic sidewalls. Construction of an insulated sidewall, which is adiabatic in nature for the scalars, temperature, and water vapor, poses an insurmountable engineering challenge. Hence, by having actively temperature controlled sidewalls, and maintaining the sidewalls at the mean temperature between top and bottom, the sidewalls are approximately adiabatic for the temperature, assuming a well-mixed fluid. For the water vapor field, the well-mixed fluid value is greater than the saturated value at the wall temperature; therefore, the zero-flux condition for water vapor cannot be achieved. Hence, to model the cloud chamber using traditional direct numerical simulation (DNS) or LES, with periodic lateral boundaries, appropriate scalar fluxes has to be provided. An approach to the budgeting of scalar fluxes for Pi Chamber is provided in section 3.1.

The Pi Cloud Chamber, in its box configuration used in the studies of (Chang et al., 2016; Chandrakar et al., 2016; Desai et al., 2018), has dimensions 2 m × 2 m × 1 m and generates turbulence by maintaining an unstable temperature gradient along the direction of gravity. To generate supersaturation inside the cloud chamber, the cold top surface and hot bottom surface are maintained at water saturation. On reaching the turbulent steady state, aerosol particles are introduced into the chamber and can act as cloud condensation nuclei (CCN) when exposed to sufficient supersaturation to form cloud droplets. A variety of instruments exist for measurement of temperature, water vapor mixing ratio, turbulence, aerosols, and cloud droplet size distributions (Chang et al., 2016; Desai et al., 2018).

The cloud chamber conditions in a typical experiment are accessible to a variety of computational approaches. On the high-fidelity side is DNS of the turbulent convection, with Lagrangian treatment of cloud droplets (e.g., Götzfried et al., 2017; Kumar et al., 2018). While this approach is being explored by several groups, it results in large computational overhead both in terms of machine resources and time. We take the more computationally efficient approach of LES for two reasons: (1) it is agile, in the sense that it allows us to explore a variety of experimental configurations with relative computational ease and (2) it is widely used in the cloud physics community, and therefore, it is of value to make direct comparison to highly constrained and well-characterized experiments. LES allows us to comprehensively explore the turbulence and microphysics throughout the volume of the cloud chamber, with relatively few assumptions or approximations imposed in obtaining boundary fluxes. In the cloud chamber, the Kolmogorov length scale is of the order of 1 mm and the droplet diameters are in the range 1–50 μm. Here we explore the possibility of studying the cloud droplet condensation growth in a turbulent environment using LES with a spatial resolution of ≈3 cm, coupled with spectral bin microphysics (SBM).

The paper is organized as follows: In section 2 we describe both the dynamics and microphysics of the LES model, including modifications to dynamics and boundary conditions made to emulate the cloud chamber. Section 3 presents the results of the study: first, we present a scalar flux budget model for calculating mean thermodynamic properties in the cloud chamber, and predicted supersaturation are explored for a range of chamber boundary conditions; second, the supersaturations predicted by the flux budget model are compared to the simulated mean properties in the LES; third, LES turbulence and flow properties are compared to known properties of Rayleigh-Bénard convection and to measurements made with particle image velocimetry (PIV); fourth, we explore the ability of LES and bin microphysics to capture various, previously published observations from the cloud chamber. Finally, the paper concludes with a summary and suggestions for next steps.

2. Description of the LES and Cloud Microphysics Model

For the LES model in this study, we use the System for Atmospheric Modeling (SAM; Khairoutdinov & Randall, 2003), which solves the equations of motion with the anelastic approximation and a 1.5 order closure based on turbulent kinetic energy (TKE) for the subgrid scales (SGS). These equations of motion are integrated using a third-order Adams-Bashforth scheme, on a fully staggered Arakawa C-type grid with uniform horizontal and vertical grid sizes. The prognostic scalars are advected using a multidimensional positive definite advection transport algorithm (Smolarkiewicz & Grabowski, 1990). Monin-Obukhov similarity theory is used to simulate surface fluxes. In standard atmospheric applications, SAM is configured to have periodic lateral boundaries and a rigid lid at the top of the domain, with Newtonian damping applied to all prognostic variables in the upper third of the model domain to reduce gravity wave reflection. For the Pi

Chamber, in addition to the bottom wall, which plays a role analogous to land surface, the top wall and lateral sides can also impose momentum and scalar fluxes. Hence, in this study, the Monin-Obukhov similarity theory is also applied at these boundaries to compute appropriate fluxes. The magnitude of the momentum fluxes is adjusted to match observed dynamical conditions in the Pi-chamber by scaling a prescribed Monin-Obukhov roughness length parameter. The mean horizontal velocity close to the top and the bottom plates is zero, hence the application of constant flux Monin - Obukhov similarity theory would yield zero flux. Therefore, the Monin-Obukhov theory is applied to individual grid boxes. Fluxes from Monin-Obukhov similarity theory were compared to and found to match those from the temperature wall function model based on Rayleigh number scaling developed by McDermott et al. (2017). Furthermore, the turbulence properties thus obtained match the experimental measurements in section 3.3. The top and bottom walls have saturated water vapor conditions at their respective temperatures, and the sidewall boundary condition is chosen to mimic the condensation processes observed during the cloud chamber experiment (further details are given in sections 3.1 and 3.2). Temperatures of the top, side, and bottom walls are all fixed.

Aerosol-cloud interactions in SAM are simulated by a SBM model described in Khain et al. (2004) and Fan et al. (2009). The SBM model involves aerosols and seven hydrometeors: water droplets, ice crystals (columnar, plate like and dendrites), snowflakes, graupel, and hail, with size distributions represented in 33 mass-doubling bins. The model accounts for relevant microphysical processes and interactions, such as activation of cloud droplets, diffusion growth or evaporation of droplets, drop collisions, turbulence effects on collisions, and collisional breakup. The presented study focuses only on warm conditions and liquid clouds, and therefore, ice microphysics is not considered in the presented simulations.

The Pi Chamber simulations presented here use a $64 \times 64 \times 32$ grid with grid spacing of 3.125 cm to simulate the 2 m $\times$ 2 m $\times$ 1 m box, for a physical time of 2 hr simulated with a 0.02 s time step. The grid spacing is at least 30 times the Kolmogorov length scale, hence the eddy cutoff for current simulations lies in the inertial range according to Monin and Yaglom (2013). The time step is chosen to satisfy the Courant-Friedrichs-Lewy (CFL) criteria. At these scales it is also possible to use underresolved DNS with numerical diffusion playing the role of molecular diffusivity, without a SGS model (Andrejczuk et al., 2004). The energy of the system can also be dissipated via numerical dissipation instead of parameterized SGS dissipation, as in the implicit LES studies conducted by Pedersen et al. (2016) and Pressel et al. (2017). However, we opted for traditional LES with SGS for scalability of the model in future. The system is initialized with a linear (unstable) temperature profile and a linear water vapor mixing ratio profile between the top and bottom walls. All velocity components are initialized to zero. The system is then allowed to spin-up to a steady state, characterized by a stable mean for TKE, SGS dissipation, relative humidity, bulk mean temperature, and bulk water vapor mixing ratio. Even though relative humidity exceeds 100% in part of the domain, no condensation occurs during the spin-up period, because initially no CCN are present. On reaching steady state, after 20 minutes of physical time, a CCN source is turned on and aerosol particles begin to be continuously added to a single grid point inside the domain, mimicking aerosol injection in the real chamber. The CCN spectrum is assumed to be monodisperse, having a mean diameter of 62.5 nm, also a typical condition in Pi Chamber experiments. The CCN, on activation grow into cloud droplets and in the presence of supersaturation, the cloud droplets grow in size and are removed by settling process. Thus, the removal mechanism for CCN is activation and for the cloud droplets is gravitational settling.

3. Results

3.1. Scalar Flux Budget Model for the Pi Chamber

We begin by introducing a flux budget model for estimating the mean supersaturation in the Pi Chamber. The model is first explored in order to understand the role of terms that are not typical in atmospheric modeling, such as the influence of sidewall heat and water vapor fluxes. Absolute measurement of supersaturation is challenging, and therefore, we rely on these fundamental calculations to aid in the evaluation of LES results for supersaturation. The comparison of the flux budget model calculations to LES results is presented in section 3.2.

The conservation law for a scalar Ψ in a volume V_0, is given by

$$\frac{\partial}{\partial t}\int_{V_0} \Psi \mathrm{d}V = \oint_{S_0} F dS, \tag{1}$$

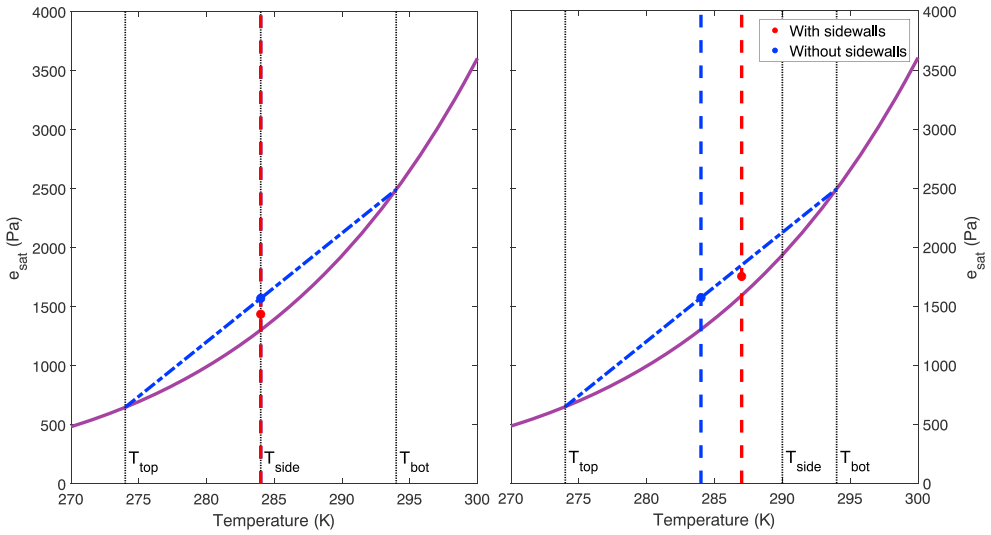

Figure 1. Water vapor pressure versus temperature, with the Clausius-Clapeyron-derived equilibrium curve (purple solid line), and line representing mixing between the bottom and top boundaries (blue dash-dotted line). The red and blue dashed lines represent the mixing temperature with and without sidewalls respectively. Left: The sidewalls are maintained at 284 K, the average of top wall and bottom wall temperatures of 274 and 294 K, respectively. The blue dashed line and red dashed line coincide in this case. Right: The sidewall temperature is 290 K, with the top and bottom temperatures at 274 and 294 K, respectively. The red and blue markers indicate the resultant mixing saturation vapor pressure for the cases with and without saturated sidewalls.

where F is the scalar flux through the bounding surface S_0. Introducing the volume-mean value $\bar{\Psi}$ and breaking S_0 into bottom, top, and sidewalls with areas A_b, A_t and A_s, respectively, we get

$$\frac{\partial}{\partial t}\bar{\Psi}V_0 = F_b A_b + F_t A_t + F_s A_s \tag{2}$$

Assuming the fluxes are driven by difference between the value of the scalar at the wall and the mean value inside the volume, that is, $F_{b/t/s} \propto (\Psi_{b/t/s} - \bar{\Psi})$. Assuming the turbulent diffusivities for all walls to be identical, equation (2) can be solved for the steady state condition, yielding

$$\bar{\Psi} = \frac{\Psi_b + \Psi_t + \hat{A}\Psi_s}{2 + \hat{A}}. \tag{3}$$

Here, we have exploited the fact that for a configuration with vertical sidewalls and parallel top and bottom planes, $A_t = A_b$, and introduced an area ratio, $\hat{A} = A_s/A_b$.

Equation (3) implies that the effect of the sidewall is scaled by the area ratio, which in case of the Pi Chamber is $\hat{A} = 2$. We also note that for a limiting case of infinite top and bottom plates, the sidewall effects disappears because $\hat{A} = 0$ and we have

$$\bar{\Psi} = \frac{\Psi_b + \Psi_t}{2}. \tag{4}$$

The same $\bar{\Psi}$ can be achieved by maintaining the sidewall value of the scalar at

$$\Psi_s = \frac{\Psi_b + \Psi_t}{2}. \tag{5}$$

The volume mean temperature and water vapor mixing ratio in the chamber calculated from equation (3) are given by

$$\bar{T} = \frac{T_b + T_t + \hat{A}T_s}{2 + \hat{A}} \tag{6}$$

and

$$\bar{Q} = \frac{Q_{\text{sat}}(T_b) + Q_{\text{sat}}(T_t) + \hat{A}Q_{\text{sat}}(T_s)}{2 + \hat{A}}, \tag{7}$$

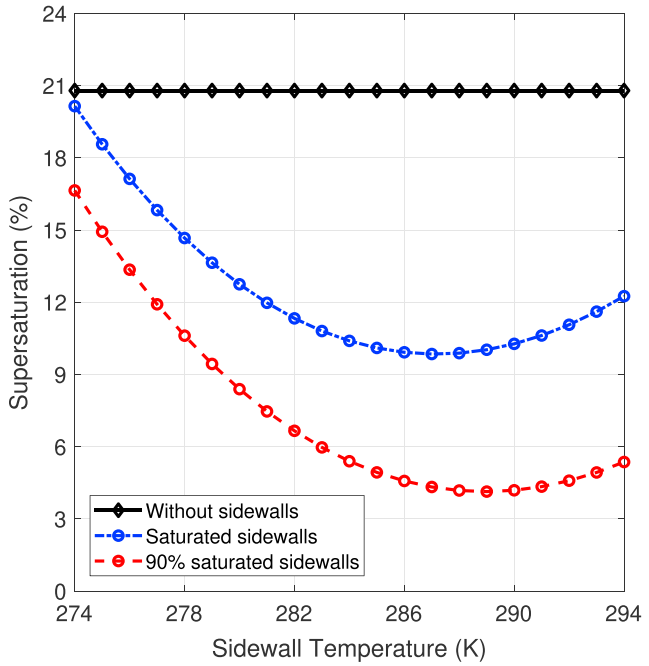

Figure 2. Supersaturation versus sidewall temperature, assuming no sidewalls (black diamonds), fully saturated sidewalls (blue circles), and slightly subsaturated sidewalls (red circles). Here, it is assumed that the top and bottom wall temperatures are 274 and 294 K, respectively.

with the assumption of water vapor being saturated at the walls at their corresponding temperatures. Because of the nonlinear dependency of Q_{sat} on T, we have $\bar{Q} > Q_{\mathrm{sat}}(\bar{T})$ and supersaturated conditions are produced, as illustrated in temperature-vapor-pressure coordinates in Figure 1. In this figure, $T_t = 274$ K and $T_b = 294$ K and two different sidewall conditions are shown. Without the sidewall contribution, the mixture properties lie on a line segment connecting bottom an top conditions (blue dash-dotted line in Figure 1). Vapor pressures on this mixing line are above the corresponding equilibrium (or saturation) vapor pressures given by the Clausius-Clapeyron equation, corresponding to the classic isobaric mixing cloud scenario (e.g., Bohren & Albrecht, 1998, sections 3.7 and 6.8). Adding sidewalls at an intermediate temperature between T_b and T_t always reduces $\bar{Q}$ and, therefore, the supersaturation of the mixture. For example, in the left panel of Figure 1 the sidewall temperature is taken as the mean value, so that equation (5) applies. The vapor pressure and temperature that would be achieved in an ideal system with no sidewalls is shown by the blue dot, and that achieved in a system with saturated sidewalls is shown by the red dot, as calculated from equations (6) and (7). The right panel of Figure 1 shows the vapor pressure and temperatures for a sidewall temperature between the mean and bottom wall temperatures.

The supersaturation is plotted as a function of sidewall temperature in Figure 2. For this figure, the top wall is maintained at $T_t = 274$ K and bottom wall at $T_b = 294$ K, and the sidewall temperatures are varied from T_t to T_b. The black diamond markers show the supersaturation without any sidewall effects and the blue circular markers indicate the resulting supersaturation from equation (3). The supersaturation graph of sidewalls with supersaturation in Figure 2 has two regimes dominated by heat flux and vapor flux respectively. The region to the left of the minimum, is dominated by heat flux. Roughly speaking, the sidewalls maintained at a lower temperature than the mean of top and bottom walls act as heat sinks and result in a reduced bulk temperature compared to the case without any sidewalls. Simulations with periodic lateral boundaries, as is typical for atmospheric applications of traditional LES and DNS, without accounting for scalar diffusivities to or from sidewalls, yields a higher supersaturation represented by the black diamond markers in Figure 2. The right-hand side of the minimum is dominated by vapor flux from the sidewalls maintained at a higher temperature than the mean of top and bottom walls. As the sidewall temperature increases, both the heat flux and vapor flux at the sidewall switches sign from negative to positive direction. The overall supersaturation decreases as the heat flux switches sign; however, it increases as the vapor flux switches sign, resulting in a minimum. A more careful derivation of the minimum point is provided in the supporting information. The important point here is that the area weighted sidewalls leads to a depletion of supersaturation compared to an infinite parallel plate case.

All the preceding discussions assumed saturated sidewalls; however, in the Pi Chamber the only source of saturation of sidewalls arises from the condensation of droplets on the sidewalls, and there are dry areas at the locations of windows. To account for this in the flux balance model, we can decrease the area of sidewalls covered with water droplets. The resulting supersaturation for a value of 90% is represented by the red circles in Figure 2, and as expected, it is lower compared to the saturated-sidewall conditions.

In practice, it is of interest to consider the conditions necessary to sustain cloud growth in the Pi Chamber, that is, to achieve a supersaturation greater than zero. Sidewall conditions that are not fully saturated (or that experience some excess heat transfer, e.g., through windows) can be compensated for either by increasing the temperature difference$\Delta T = T_b - T_t$ or by adjusting the sidewall temperature T_s. The two effects are illustrated in Figure 3, which shows the minimum sidewall saturation ratio necessary to attain relative humidity of 100% (or zero supersaturation) in the Pi Chamber. The red axis and curve show the ratio as a function of ΔT, and the blue axis and curve show the ratio as a function of T_s. At lower ΔT, we can see that a sidewall saturation ratio closer to 100%, implying a fully saturated sidewall is required to yield supersaturation. As the temperature difference increases to 20 K, a sidewall saturation ratio as low as 80% can

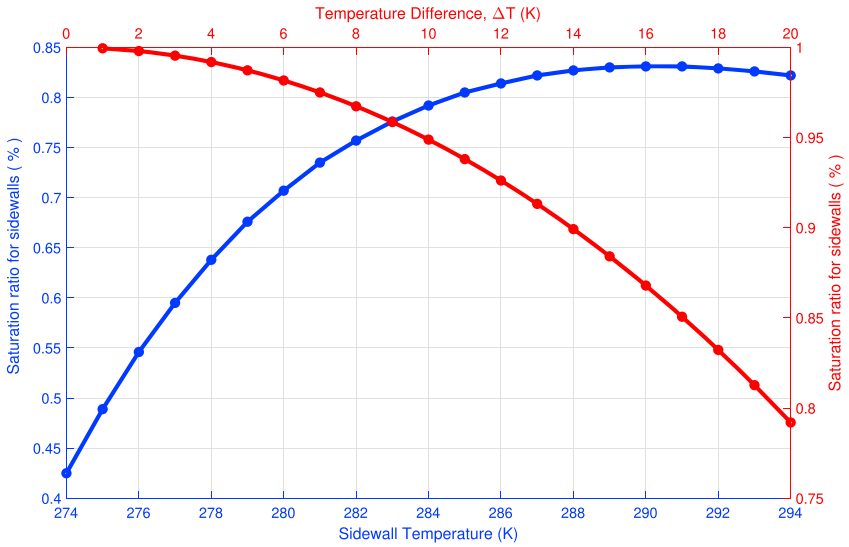

Figure 3. Red: Minimum saturation ratio at the sidewall required for 100% relative humidity in the cloud chamber, versus temperature difference, ΔT. Here the sidewall temperature is kept at the mean bulk temperature of 284 K. Larger ΔT is required to compensate for drier sidewalls, in order to maintain cloud-sustaining conditions. Blue: Minimum saturation ratio at the sidewall required for 100% relative humidity in the cloud chamber, versus the sidewall temperature. Here the temperature difference, ΔT is kept constant at 20 K and the sidewall temperatures are changed from 274 to 294 K. A derivation describing these two curves is provided in the supporting information.

yield supersaturation. Hence at higher temperature differences, it is easier to attain supersaturation, even if the sidewalls are not fully saturated. The blue curve shows that this can be further adjusted by varying the sidewall temperature, as was implied in the earlier discussion.

3.2. Scalar Flux Budget Model Compared With LES Results

The flux budget model suggests that the mean supersaturation attained in the Pi Chamber depends on a combination of ΔT and T_s. This provides a reference for interpreting the mean state calculated with the LES. In this section, all LES results are for the thermodynamic state of the turbulent mixture of air and water vapor, with no cloud formation. Figure 4 is obtained by varying saturated sidewall temperature from T_t to T_b, for fixed ΔT. Panels showing the mean fluid temperature, water vapor mixing ratio, and relative humidity are shown. The blue circles are the results from the flux model and the red squares are from the LES, both for $\Delta T = 20$ K and with T_s increments of 2 K.

The results in Figure 4 show reasonable consistency between the trends from the LES and the predictions of the relatively simple flux balance model. The mixing temperature and water vapor mixing ratio, for varying sidewalls are shown in the top two panels of Figure 4. For temperature and water vapor, we can see that the scalar flux model predicts slightly higher values than LES for higher sidewall temperatures and slightly lower values than LES for lower sidewall temperatures. Encouragingly, the crossover occurs at a temperature very close to the mean of T_b and T_t, $T_s = 284$ K. The offsets at smaller and larger T_s are likely due to the assumption of uniform turbulent diffusivities for top wall, bottom wall, and sidewall in the simple scalar flux model. The relatively small discrepancies in temperature and water vapor mixing ratio result in lower supersaturation for the LES at lower T_s than predicted by the scalar flux model. Conversely, the lower mixing temperatures at higher sidewall temperatures result in a higher supersaturation for LES than the scalar flux model at larger T_s. These trends in supersaturation are evident in the third panel of Figure 4. Again, the scenario with sidewall temperature at the mean of the top and bottom boundary temperatures serves as a check (cf. equation (5)) and indeed, the supersaturation from the LES matches the prediction of the scalar flux model quite well.

Accurate experimental measurement of supersaturation and water vapor inside the cloud chamber is a matter of continuing effort, but based on the activated fraction of aerosols, and mean cloud droplet diameters, the supersaturation can be estimated as close to 1–2% for $\Delta T \approx 19$ K and the configuration used in several recent experiments (Chandrakar et al., 2016, 2017, 2018). In order to achieve these values of supersaturation in the LES, the sidewall saturation ratio is reduced for the simulations analyzed below. For chamber boundary

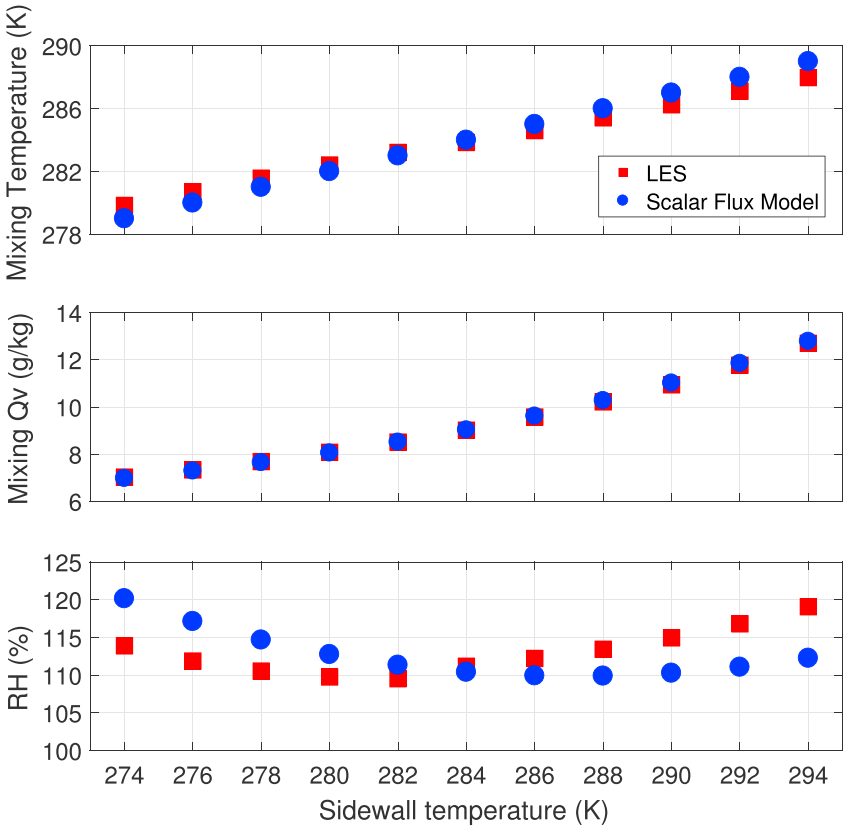

Figure 4. Comparison of mixing temperature, water vapor mixing ratio, and relative humidity (RH) versus sidewall temperature, as calculated from the scalar flux budget model (blue circles) and the large-eddy simulation (LES, red squares). Results are shown for a temperature difference of $\Delta T = 20$ K with top and bottom boundaries at 274 and 294 K, respectively. LES values are obtained by averaging over the full volume, excluding grid points close to the sidewall boundaries, and averaging in time from 1,800 to 3,600 s.

temperatures of $T_t = 280$ K, $T_b = 299$ K, and $T_s = 285$ K, that is, $\Delta T = 19$ K, equations (6) and (7) show that a sidewall saturated fraction of 0.74 is required to achieve 100% RH. The same set of equations predict a RH of 102.5% with a saturated fraction of 0.80. We then iterate to determine that this RH is achieved in the LES with a sidewall saturated fraction of 0.82, and this value is used in the subsequent work.

3.3. LES Turbulence and Flow Properties

In this subsection we describe the flow and turbulence properties of the convection, as captured by the LES. Particle-image velocimetry measurements are also described and compared to the LES in order to evaluate the model performance.

Figure 5 shows the time-averaged temperature and water vapor mixing ratio profiles along the axis of gravity for the conditions before and after aerosol injection. As expected for turbulent Rayleigh-Bénard convection, the temperature and the mixing ratio remain relatively constant throughout the bulk of the chamber due to the efficient mixing of the turbulence. The strongest gradients in temperature and water vapor mixing ratio are found near the top and bottom boundaries. In Figure 5 we can see that the temperature profile shifts to the right when aerosol is introduced and a cloud is formed, indicating an increase in temperature, owing to the latent heat release due to the condensation growth of cloud droplets. This process in turn decreases the available water vapor in the bulk causing the mixing ratio curves to shift to the left as illustrated in the figure.

The TKE, energy dissipation rate ϵ, and the frequency of oscillations of the large-scale circulation are measures of the convective turbulence inside the chamber (Niedermeier et al., 2018). Matching TKE and ϵ from the LES with experimental results indicates that the boundary fluxes are properly evaluated. We use PIV to visualize and measure the two-dimensional velocity field at the center of the chamber. A 200-mW CW laser is used in combination with a laser-line-generator lens to illuminate a sheet of droplets at the center of the chamber. The illuminated droplets are recorded using a CCD camera (Alpha 7S2, Sony) at a framerate

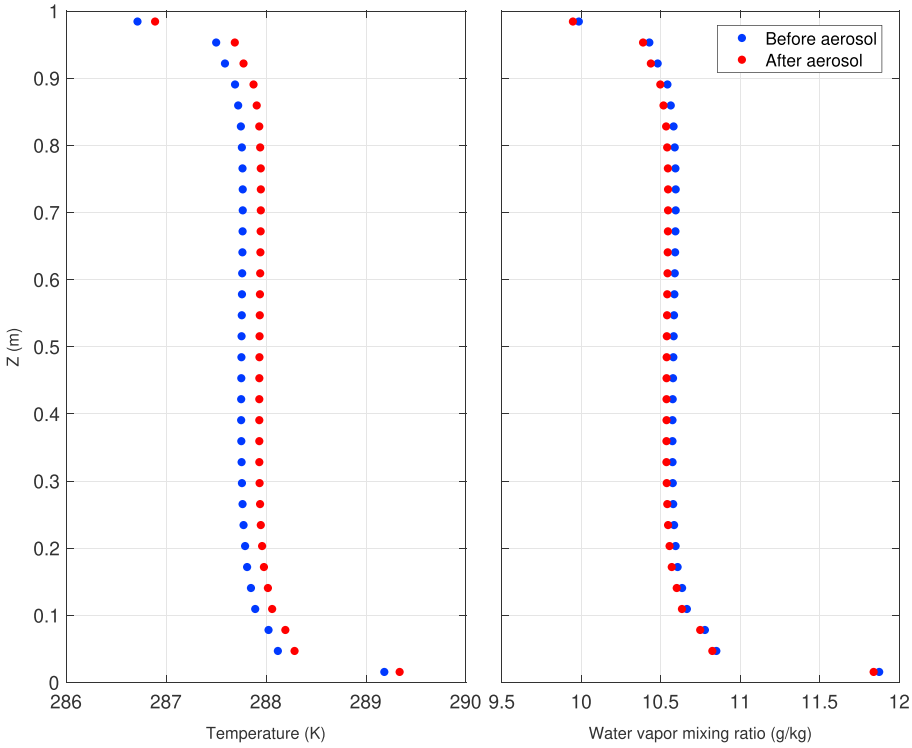

Figure 5. Vertical profiles of horizontally averaged temperature and water vapor mixing ratio. Profiles are shown for cloud-free, that is, no aerosol particles, conditions (red circles), for a temperature difference of 20 K with T_b, T_s, T_w at 294, 284, and 274 K, respectively. The results are obtained by averaging over time from 1,800 to 3,600 s in the chamber simulation.

of 120 fps and a resolution of $1,920 \times 1,080$ pixels at ≈60–100 μm per pixel, depending on the field of view (20×10 to 10×5 cm^2). By using the cloud droplets as a fluid tracer, no additional particulates (such as oil droplets, or polymer powder) have to be introduced into the cloud environment. This requires that the Stokes number of the droplets, $St = \tau_d/\tau_\eta$ is very small, where $\tau_d = \rho_l d^2/18\nu\rho_a$ is the droplet response time and $\tau_\eta = (\nu/\varepsilon)^{1/2}$ is the turbulence dissipation eddy time scale. Here ρ_a and ρ_l are mass densities for air and liquid water, respectively, and ν is the kinematic viscosity of air. For the droplet distributions used in this experiment, assuming an (expected) dissipation rate $\varepsilon \approx 10^{-3}$ m^2 s^{-3} (Chang et al., 2016), the Stokes number results vary on the order of $10^{-5} - 10^{-3}$, and therefore, droplets serve as reasonable tracers.

To obtain a converged estimate of the turbulence statistics, the camera records the droplet dynamics for approximately an hour for each condition measured. Image pairs at a time delay of $\Delta t = 1/120$ s are sampled at 2 Hz, resulting in approximately 2,500–4,000 image pairs per experiment (accounting for adequate averaging). Commercial PIV software (Pivtec, PIVTEC Gmbh) was used to process the images. PIV correlation windows of 48×48 and 64×64 pixels are used, depending on the droplet number concentration and field of view, with a consistent window overlap of 50%.

To determine the TKE, the root-mean-square of the droplet velocity components (in both horizontal (u) and vertical (w) directions) are averaged over the available data, that is, $U = \sum (u^2 + w^2)^{1/2}$, where the sum is taken over the full PIV window and all available image pairs.

The dissipation rate ε can be estimated using the Smagorinsky turbulence model from the measured velocity gradients in the PIV. As the measurement has a limited resolution, the minimum PIV window size (5 cm) is 50 times larger than the Kolmogorov length (1 mm) of the small-scale turbulent eddies. This results in an inherent filtering of the turbulent velocity field, which requires a correction of the resulting dissipation rate, detailed by Bertens et al. (2015). This correction, based on the size of the PIV window to the Kolmogorov scale η, gives an uncertainty ≈25% in homogeneous, isotropic turbulence. It should also be noted that the turbulence in Rayleigh-Bénard convection is somewhat anisotropic, so the equipartition of TKE is not strictly valid and therefore we make the comparison of PIV and LES results in 2-D.

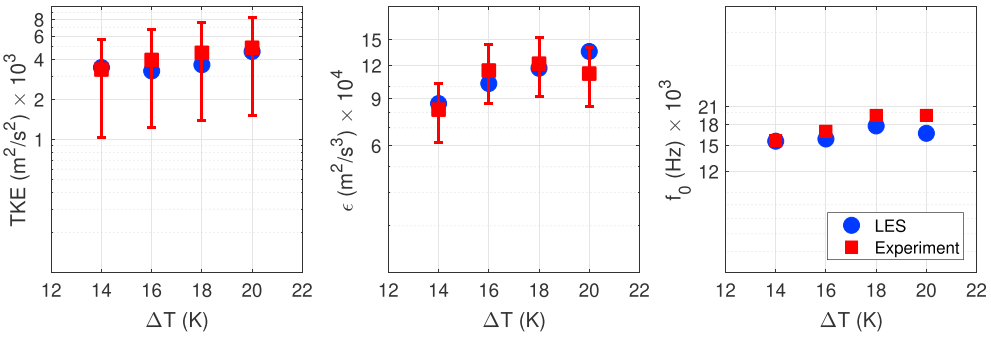

Figure 6. Turbulent kinetic energy (TKE), eddy dissipation rate (ϵ), and large-scale oscillation frequency versus temperature difference ΔT. The large-eddy simulation (LES) results are shown by the blue circles and the experimental results by the red squares. The LES results are time averaged between 1,800 and 3,600 s. The 2-D TKE is calculated from the u and w velocity fluctuations, and similar to the experimental results, the effect of large-scale oscillations are filtered by subtracting a moving mean over 1 min from the point measurements in the simulation. The ϵ is obtained from the center plane and the large-scale oscillation frequency is obtained from the Fourier transform of point temperature measurements in the simulation.

The left two panels of Figure 6 show the comparison of the average TKE and ϵ for LES (blue circles) and experiments (red squares), for four different values of ΔT. As expected, in the experiments both the TKE and consequently the energy dissipation rates increase as the temperature difference is increased. The LES captures a quantitatively similar trend. The TKE and ϵ from the simulations are slightly higher than the experimental observations, but within the experimental uncertainties.

The presence of a coherent, large-scale circulation in Rayleigh-Bénard convection within the Pi Chamber has been documented by Niedermeier et al. (2018). Encouragingly, the LES also produces a large-scale circulation, and it is observed to experience oscillations similar to the experiments. To determine the frequency of large-scale oscillation in the LES, a Fourier analysis is performed on the temperature sampled at 50 Hz from a point at the center of the chamber. From the frequency spectra thus obtained, the maximum between 0.1 and 0.01 Hz is identified as the large-scale oscillation frequency (an example of a frequency spectrum is shown Figure S1 in the supporting information). As shown in the right panel of Figure 6, the LES is able to qualitatively, and even to some extent quantitatively capture the frequencies measured in the cloud chamber experiments.

3.4. Simulated Steady-State Cloud

A primary motivation for experiments in the Pi Chamber is to study aerosol-cloud-turbulence interactions in a controlled environment (Chang et al., 2016). For example, (Chandrakar et al., 2016, 2018) found that the width of cloud droplet size distribution increases with a decreasing aerosol injection rate, and this broadening is due to a combination of mean and variability in the diffusional growth of cloud droplets in a turbulent environment, rather than broadening due to the collision-coalescence process. However, there is only indirect observational evidence to support the predominant role of condensation growth including a significant contribution from turbulence, as well as the absence of collisions in the chamber. This is because the growth history of individual cloud droplets is unknown (and currently unobservable), and only the distribution properties are known. The modified cloud-resolving LES in this study provides a useful tool to study the relative roles of condensation and collisions in the growth process, and on the cloud droplet size distribution in the cloud chamber.

Here we present the results of the simulated steady-state clouds in detail, as a parallel study to (Chandrakar et al., 2016, 2018). The scientific questions we want to address are (1) can the model simulate the microphysical properties of steady-state clouds? (2) do simulations reproduce the broadening of cloud droplet size distribution with the decrease of cloud droplet number concentration? (3) does the collision-coalescence process really play a negligible role in droplet growth in the chamber? It should be mentioned that this model can also be applied to investigate several other processes, including cloud cleansing and collapse (Chandrakar et al., 2017), and the influence of variable cloud microphysical properties on stochastic condensation (Desai et al., 2018). Simulations under those conditions will be investigated in the future. For this paper, our purpose

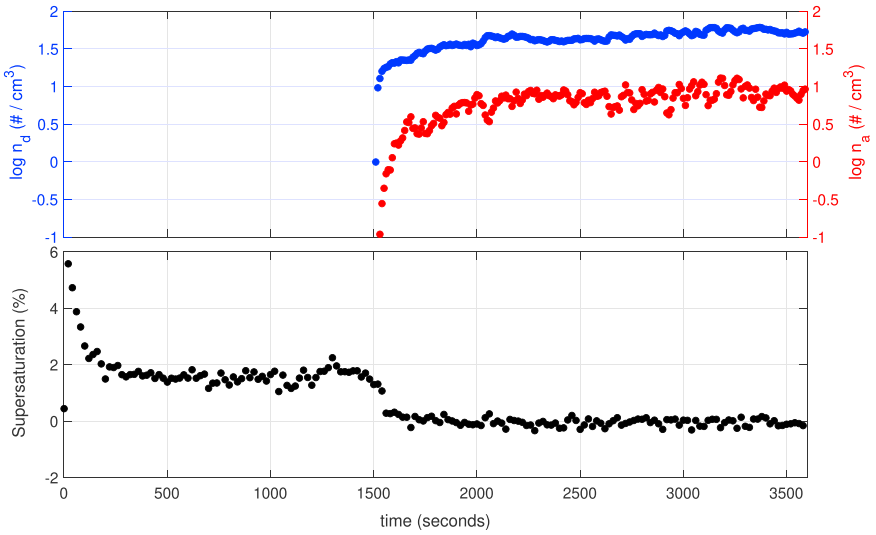

Figure 7. Time series of cloud droplet number density (top panel, blue circles), aerosol concentration (top panel, red circles), and supersaturation (bottom panel, black circles). Up to a time of 1,500 s no aerosols or cloud droplets are present, and at 1,500 s a steady injection rate of aerosol particles is initiated. The plots are volume-averaged droplet concentration, cloud condensation nuclei concentration, and supersaturation, excluding the grid points close to the boundaries.

is to demonstrate that previously published, steady-state microphysical results can be reasonably replicated by the LES.

The simulation is set up with a temperature difference of 19 K, with bottom, top and sidewall temperatures set to 299, 280, and 285 K, respectively. The cloud box is modeled with a grid size of 3.125 cm and a step size of 0.02 s. The top and bottom walls are saturated and the sidewall saturation ratio is set to 0.82 to ensure a mean supersaturation of 2.5% when no cloud droplets are present. The cloud microphysical processes are simulated using a bin microphysical scheme (Khain et al., 2004). There are 33 mass-doubling bins for aerosol and 33 mass-doubling bins for cloud droplets. Aerosol particles in one bin are activated as cloud droplets if their critical supersaturation is smaller than the environmental supersaturation in that grid box, based on Köhler theory. Diffusional growth, collisional growth, and sedimentation of cloud droplets are considered. To mimic the constant aerosol injection rate during the experiments (Chandrakar et al., 2016, 2018), a point source of monodisperse aerosol with a fixed number concentration is added at the center of the simulation domain. It should be mentioned that instead of injecting aerosol in the simulation domain, we forced a constant aerosol number concentration in one grid box (at the center). This is because the current LES model and microphysical scheme lack two important sinks for aerosols: cloud scavenging and wall loss. Without those processes, the simulated aerosol number concentration will continuously increase with time for a constant aerosol injection rate, which is not consistent with the observed steady-state aerosol number concentration in the cloud chamber. (In experiments, steady state conditions in cloud properties are reached before steady state conditions in aerosol concentration because of the differing sinks for the two; see, e.g., Figure 1 in Chandrakar et al., 2017.) The total simulation time is one hour: without aerosol input for the first half an hour and with aerosol input for the second half an hour.

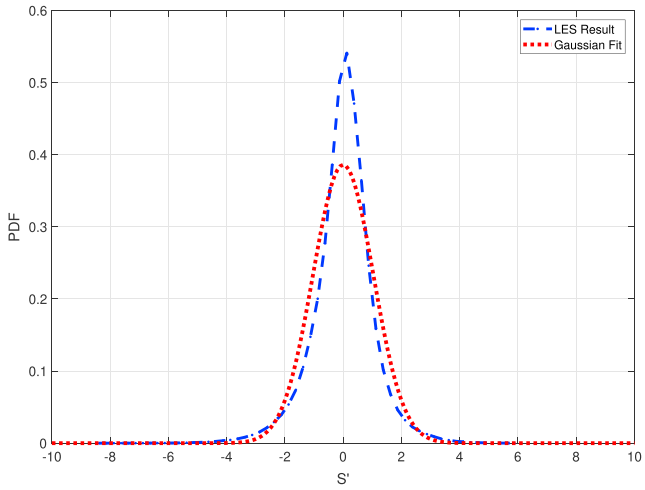

Figure 8. The probability density function (PDF) of supersaturation fluctuations at the center of the chamber, with no aerosol injection. The standard deviation is 1.033. The measurements are from spatial and temporal averages within the simulated chamber. The kurtosis of the supersaturation is 5.7, greater than 3 for Gaussian, implying greater excursions of supersaturation fluctuation from the normal distribution.

Figure 7 shows the time series of the domain-averaged cloud droplet number concentration, aerosol number concentration, and relative humidity for one cloud simulation with an aerosol source number concentration of 3,697 cm^{-3} for the bin centered at 62.5-nm diameter at the center of the chamber. It can be seen that cloud does not form without aerosol input within the first half an hour, even though the relative

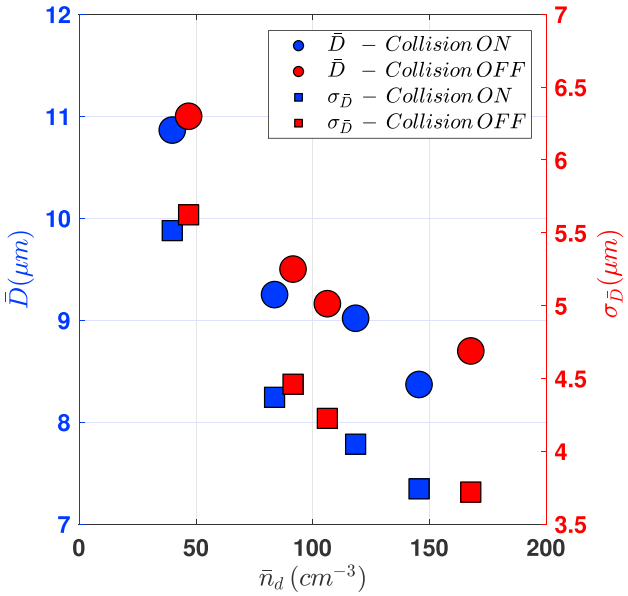

Figure 9. Mean (circles) and standard deviation (squares) of cloud droplet diameter versus cloud droplet concentration.Blue symbols denote collisions on and red symbols denote collisions off. The relative dispersion ($\sigma_r/\bar{r}$) varies from 0.51 to 0.42 with increasing cloud droplet concentration for cases with collisions off. Size distributions are obtained from the number per bin at each grid point in the bulk of the chamber for a single snapshot, and mean and standard deviations are calculated from the distributions.

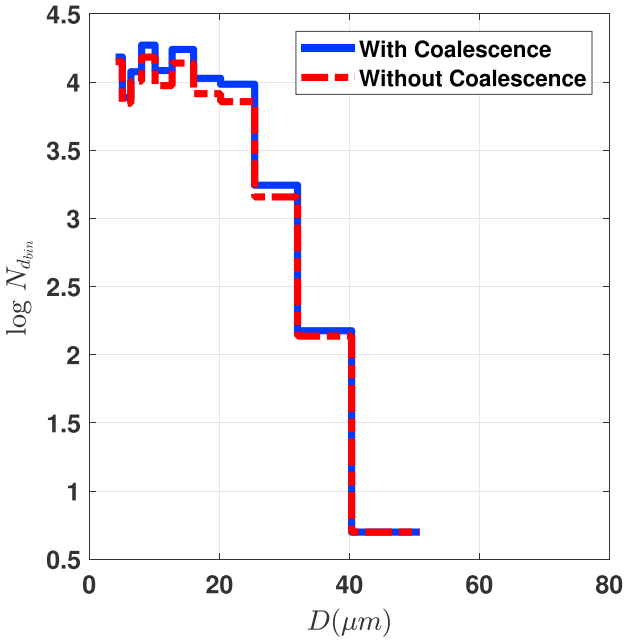

Figure 10. Number of droplets observed in the cloud chamber simulation versus the diameter for one set of aerosol conditions. The collision-coalescence physics is turned on and off in the simulations for blue and red, respectively. The distribution is obtained from the number of droplets per bin at each grid point in the bulk of the chamber, for a single snapshot.

humidity is above 100%. The domain-averaged relative humidity reaches a steady state of about 102% after about 100 s. Relative humidity varies due to fluctuations in temperature and water vapor within the turbulent environment (Siebert & Shaw, 2017). The probability density function (PDF) of supersaturation fluctuations ($s' = s - \bar{s}$) at the center of the chamber without aerosol input is similar to a Gaussian distribution, as shown in Figure 8. This is consistent with the observational results (Chandrakar et al., 2016) and the assumptions made in several additional studies (Chandrakar et al., 2017, 2018; Desai et al., 2018). It should be noted, however, that the LES suggests a somewhat more intermittent distribution than Gaussian, with a kurtosis of 5.7; this departure and its possible implications will be interesting topics for an additional study in the future. When aerosols are introduced to the simulation domain, the relative humidity decreases as expected due to the formation and growth of cloud droplets (bottom panel of Figure 7). Cloud droplet number concentration, aerosol number concentration, and the relative humidity reach a steady state, consistent with the observations (Chang et al., 2016). Finally, the PDF of supersaturation fluctuations after the cloud has formed becomes narrower, as expected (see Figure S2 in the supporting information).

To investigate the influence of aerosol concentration on the cloud droplet size distribution, we did sensitivity studies by changing the aerosol number concentration of the point source. Four different aerosol number concentrations were implemented by maintaining concentrations of 3,697, 5,545, 7,394, and 9,242 cm^{-3} at the center of the chamber. The mean and standard deviation of cloud droplet diameter during the steady state, as obtained from both a temporal and spatial average, are calculated for each case. Figure 9 shows that both the mean and the standard deviation of droplet size decrease with increasing cloud droplet number concentration, which is consistent with the observations of (Chandrakar et al., 2016, 2018). The trends are consistent, but the exact values of mean diameter and standard deviation do not closely match the observational results (e.g., Table 1 in Chandrakar et al., 2016), especially for relatively clean conditions, where the simulated mean diameter and standard deviation are both smaller than the observations. This might be due to the different averaging procedures in LES versus experiment, the differences in injected aerosol size distribution, the measurement uncertainties, or the inaccurate representation of either dynamics or microphysics or both. A careful investigation of this will be carried out in the future. Finally, we note that examples of size distributions due to aerosol injection are shown in Figure S3 in the supporting information file.

The LES model can simulate and maintain a steady-state cloud by adding a source of aerosol with a constant aerosol number concentration (cf. Figure 7). Modeling results also show the broadening of cloud droplet size distribution with the decrease of cloud droplet number concentration (Figure 9). These results are consistent with observations (Chang et al., 2016; Chandrakar et al., 2016), implying that the cloud-resolving LES model captures the essential cloud microphysical properties in the convection chamber. An additional question is, does the collision-coalescence process contribute to the observed broadening of the droplet size distribution? In order to answer this question, we did another set of simulations without the collision-coalescence process. An example result is shown in Figure 10, corresponding to an aerosol concentration of 5,545 cm^{-3} at the center of the chamber and a steady-state cloud droplet concentration of 40 cm^{-3} without coalescence and 47 cm^{-3}

with coalescence. The results, which are representative of the other cases, show that the shape of the cloud droplet size distribution does not change significantly without the collision-coalescence process. This confirms that the width of the droplet size distribution is primarily a result of the vapor condensation process. The small change in droplet concentration observed between the with and without coalescence runs is intriguing and is the topic of ongoing study. We note, however, that the estimate of mean diameter varies spatially and temporally, so determining what differences are a result of statistical fluctuations versus actual changes in mean properties, will require careful averaging. For example, for the results shown in Figure 9, the standard deviation of the estimate of the mean diameter, estimated from spatial variations at one time, is between 0.2 and 0.5 μm. Thus, interpreting the small changes in distribution shape when collisions are included or not, will require longer averaging.

4. Summary and Discussion

The SAM code coupled with spectral bin cloud microphysics has been modified to simulate conditions in the Pi Chamber. To accommodate the presence of the lateral and top walls, momentum and scalar fluxes are implemented using Monin-Obukhov similarity with the roughness parameter scaled for quantitative matching. The top and bottom walls are held at saturated conditions and at constant temperatures during the simulations, with an unstable temperature difference that drives turbulent Rayleigh-Bénard convection. The lateral walls are prescribed a saturated fraction to achieve realistic supersaturation levels consistent with the condensation growth observed in the cloud chamber experiments.

A flux balance model is introduced to quantify the steady state scalar values, and this model is used to explore the supersaturations achieved by treating temperature and water vapor mixing ratio as independent scalars. The presence of the sidewalls decrease the supersaturation from the maximum attainable values for an idealized condition with no sidewalls. The supersaturation thus attained can be further decreased by the presence of an additional heat flux or partially saturated sidewalls. The trend predicted by the flux balance model is faithfully replicated by the LES model.

With these changes to SAM, the results from the simulation agree adequately with the experiments in terms of dynamics and microphysical properties. The dynamics, measure by TKE, turbulence energy dissipation rate, and oscillation frequency of the large-scale circulation are within the uncertainty range of experiments. Furthermore, key microphysical behaviors observed in experiments with the Pi Chamber are able to be reproduced in the simulations. Specifically, steady-state microphysical conditions are achieved for a constant injection of aerosol particles to the chamber; the supersaturation field in the cloud chamber shows an approximately Gaussian distribution; mean and standard deviation of the cloud droplet size distribution increase monotonically with decreasing cloud droplet number density; and finally, the droplet growth is dominated by condensation rather than collisions for typical conditions in the cloud chamber. Taken together, these results imply that there is reasonable scalability of the LES model and the microphysical processes to the laboratory context.

The initial motivation for developing a LES of the convection and aerosol-cloud interactions in the Pi Chamber was to more deeply understand and interpret laboratory observations, which are usually Eulerian in nature and do not provide easy access to some important variables, like absolute water vapor supersaturation (water vapor fluctuations can be more reliably quantified). But as the work progressed we began to see it in a broader context. First, LES provides an excellent opportunity to scale processes and results observed in the laboratory to a more realistic atmospheric context. In that sense, it is especially compelling to perform this study with a model like SAM that is widely used in the cloud community.

Second, and perhaps more ambitiously, LES not only can inform the experiments and allow for rescaling of results but also provides an opportunity to evaluate and even, at some stage, to validate numerical models for turbulence and microphysics. Simply put, intercomparison with a steady-state laboratory flow with known boundary conditions, and carefully measured properties, allows LES and bin microphysics to be compared to experiment with a level of detail and precision heretofore not possible. The atmospheric-boundary-layer community has a history already of synergy between laboratory experiments and LES (Fedorovich & Thäter, 2001; Fedorovich et al., 2001a, 2001b; Wyngaard, 1998a). Furthermore, the need for such intercomparison has been emphasized. For example, Stevens and Lenschow (2001) pointed out the need for "initiatives to develop symbiotic relationships between observations, experiments, and LES" and Wyngaard (1998b) particularly emphasized the role of laboratory experiments: "A remaining and not widely acknowledged problem

is the great difficulty of testing the fidelity and reliability of the LES results. Here laboratory flows can serve as ground truth, since they generally provide 'cleaner', less scattered data than the atmosphere itself." The cloud physics community, in contrast, has long relied on laboratory experimentation for the investigation of fundamental processes, often linked to single particles, such as ice nucleation or collision efficiencies. But to our knowledge, there has been little discussion of the potential benefits of comparing the observed dynamics of ensembles of aerosol and cloud hydrometeors within a turbulent flow directly with cloudy LES. In that regard, we consider this as a first, tentative step, with emphasis on description of the LES model as applied to the Pi Chamber, and sufficient evaluation of the flow dynamics and cloud microphysical properties to provide support for the further study. Many opportunities for detailed intercomparison focused on specific problems now are possible: the role of supersaturation mean and fluctuations on the broadening of size distributions, and the role of collision-coalescence under varying aerosol conditions stand out as examples. For the purposes of the current study, the default bins from HUJISBM are sufficient to capture the general trends observed in the experiments. However, to study other aspects of aerosol-cloud interactions, such as, for example broadening of DSD due to Ostwald ripening (Yang et al., 2018), one might have to rely on other approaches such as 2-D bin microphysics (Lebo & Seinfeld, 2011; Ovchinnikov & Easter, 2010). Grabowski et al. (2018) have pointed out the challenges in modeling cloud microphysics using the popular bulk and bin methods, including the effect of numerical diffusion both in radius space and vertical advection causing artificial broadening, and they propose Lagrangian particle methods described by (Andrejczuk et al., 2008; Riechelmann et al., 2012; Shima et al., 2009; Sölch & Kärcher, 2010) as a promising way forward. Thus, a potential extension of the current work would be to explore cloud chamber modeling using Lagrangian particles and an intercomparison with a laboratory validated LES study presented in this paper.

Acknowledgments
This work was supported by National Science Foundation Grant AGS-1754244. Part of this work was completed during visits by Subin Thomas and Fan Yang to the Pacific Northwest National Laboratory (PNNL) under the Alternate Sponsored Fellowship Program. Mikhail Ovchinnikov was supported by the U.S. DOE Office of Science Atmospheric System Research (ASR) program. The PNNL is operated for DOE by Battelle Memorial Institute under contract DE-AC05-76RLO1830. The SAM model is available from Marat Khairoutdinov of Stony Brook University (http://rossby.msrc.sunysb.edu/~marat/SAM.html). Measurement and simulation results in the figures are available at https://digitalcommons.mtu.edu/physics-fp/155/ website. Portage, a high-performance computing infrastructure at Michigan Technological University, was used in obtaining results presented in this publication. We thank Kamal Kant Chandrakar and Greg Kinney for assistance in making measurements that are compared with the LES. We thank Wojciech Grabowski and an anonymous reviewer for their helpful comments.

References

Andrejczuk, M., Grabowski, W. W., Malinowski, S. P., & Smolarkiewicz, P. K. (2004). Numerical simulation of cloud–clear air interfacial mixing. *Journal of the atmospheric sciences*, *61*(14), 1726–1739.

Andrejczuk, M., Reisner, J., Henson, B., Dubey, M., & Jeffery, C. (2008). The potential impacts of pollution on a nondrizzling stratus deck: Does aerosol number matter more than type? *Journal of Geophysical Research*, *113*, D19204. https://doi.org/10.1029/2007JD009445

Bertens, A., van der Voort, D., Bocanegra Evans, H., & van de Water, W. (2015). Large-eddy estimate of the turbulent dissipation rate using PIV. *Experiments in Fluids*, *56*, 1–9.

Bohren, C. F., & Albrecht, B. A. (1998). *Atmospheric Thermodynamics*. New York: Oxford Univ. Press.

Chandrakar, K. K., Cantrell, W., Chang, K., Ciochetto, D., Niedermeier, D., Ovchinnikov, M., et al. (2016). Aerosol indirect effect from turbulence-induced broadening of cloud-droplet size distributions. *Proceedings of the National Academy of Sciences*, *113*(50), 14,243–14,248.

Chandrakar, K., Cantrell, W., Ciochetto, D., Karki, S., Kinney, G., & Shaw, R. (2017). Aerosol removal and cloud collapse accelerated by supersaturation fluctuations in turbulence. *Geophysical Research Letters*, *44*, 4359–4367. https://doi.org/10.1002/2017GL072762

Chandrakar, K., Cantrell, W., & Shaw, R. (2018). Influence of turbulent fluctuations on cloud droplet size dispersion and aerosol indirect effects. *Journal of the Atmospheric Sciences*, *75*(9), 3191–3209.

Chang, K., Bench, J., Brege, M., Cantrell, W., Chandrakar, K., Ciochetto, D., et al. (2016). A laboratory facility to study gas–aerosol–cloud interactions in a turbulent environment: The π chamber. *Bulletin of the American Meteorological Society*, *97*(12), 2343–2358.

Chillà, F., & Schumacher, J. (2012). New perspectives in turbulent Rayleigh-Bénard convection. *The European Physical Journal E*, *35*(7), 58.

Deardorff, J. W. (1980). Stratocumulus-capped mixed layers derived from a three-dimensional model. *Boundary-Layer Meteorology*, *18*(4), 495–527.

Desai, N., Chandrakar, K., Chang, K., Cantrell, W., & Shaw, R. (2018). Influence of microphysical variability on stochastic condensation in a turbulent laboratory cloud. *Journal of the Atmospheric Sciences*, *75*(1), 189–201.

Fan, J., Ovtchinnikov, M., Comstock, J. M., McFarlane, S. A., & Khain, A. (2009). Ice formation in arctic mixed-phase clouds: Insights from a 3-D cloud-resolving model with size-resolved aerosol and cloud microphysics. *Journal of Geophysical Research*, *114*, D04205. https://doi.org/10.1029/2008JD010782

Fedorovich, E., Nieuwstadt, F., & Kaiser, R. (2001a). Numerical and laboratory study of a horizontally evolving convective boundary layer. Part I: Transition regimes and development of the mixed layer. *Journal of the Atmospheric Sciences*, *58*(1), 70–86.

Fedorovich, E., Nieuwstadt, F., & Kaiser, R. (2001b). Numerical and laboratory study of horizontally evolving convective boundary layer. Part II: Effects of elevated wind shear and surface roughness. *Journal of the atmospheric sciences*, *58*(6), 546–560.

Fedorovich, E., & Thäter, J. (2001). Vertical transport of heat and momentum across a sheared density interface at the top of a horizontally evolving convective boundary layer&dag. *Journal of Turbulence*, *2*(1), 007–007.

Götzfried, P., Kumar, B., Shaw, R. A., & Schumacher, J. (2017). Droplet dynamics and fine-scale structure in a shearless turbulent mixing layer with phase changes. *Journal of Fluid Mechanics*, *814*, 452–483.

Grabowski, W. W., Morrison, H., Shima, S.-i., Abade, G. C., Dziekan, P., & Pawlowska, H. (2018). Modeling of cloud microphysics: Can we do better? *Bulletin of the American Meteorological Society*, *100*(4), 655–672.

Khain, A., Ovtchinnikov, M., Pinsky, M., Pokrovsky, A., & Krugliak, H. (2000). Notes on the state-of-the-art numerical modeling of cloud microphysics. *Atmospheric Research*, *55*(3-4), 159–224.

Khain, A., Pokrovsky, A., Pinsky, M., Seifert, A., & Phillips, V. (2004). Simulation of effects of atmospheric aerosols on deep turbulent convective clouds using a spectral microphysics mixed-phase cumulus cloud model. Part I: Model description and possible applications. *Journal of the atmospheric sciences*, *61*(24), 2963–2982.

Khairoutdinov, M. F., & Kogan, Y. L. (1999). A large eddy simulation model with explicit microphysics: Validation against aircraft observations of a stratocumulus-topped boundary layer. *Journal of the atmospheric sciences*, *56*(13), 2115–2131.

Khairoutdinov, M., & Kogan, Y. (2000). A new cloud physics parameterization in a large-eddy simulation model of marine stratocumulus. *Monthly weather review*, *128*(1), 229–243.

Khairoutdinov, M. F., Krueger, S. K., Moeng, C.-H., Bogenschutz, P. A., & Randall, D. A. (2009). Large-eddy simulation of maritime deep tropical convection. *Journal of Advances in Modeling Earth Systems*, *1*, 15. https://doi.org/10.3894/JAMES.2009.1.15

Khairoutdinov, M. F., & Randall, D. A. (2003). Cloud resolving modeling of the arm summer 1997 IOP: Model formulation, results, uncertainties, and sensitivities. *Journal of the Atmospheric Sciences*, *60*(4), 607–625.

Kogan, Y., Khairoutdinov, M., Lilly, D., Kogan, Z., & Liu, Q. (1995). Modeling of stratocumulus cloud layers in a large eddy simulation model with explicit microphysics. *Journal of the Atmospheric Sciences*, *52*(16), 2923–2940.

Kumar, B., Götzfried, P., Suresh, N., Schumacher, J., & Shaw, R. A. (2018). Scale dependence of cloud microphysical response to turbulent entrainment and mixing. *Journal of Advances in Modeling Earth Systems*, *10*, 2777–2785. https://doi.org/10.1029/2018MS001487

Lebo, Z., & Seinfeld, J. (2011). A continuous spectral aerosol-droplet microphysics model. *Atmospheric Chemistry and Physics*, *11*(23), 12,297–12,316.

McDermott, R., Vanella, M., & Henderson, B. (2017). A temperature wall function for large-eddy simulation of natural convection based on modified Rayleigh number scaling. APS Meeting Abstracts.

Moeng, C.-H. (1986). Large-eddy simulation of a stratus-topped boundary layer. part I: Structure and budgets. *Journal of the atmospheric sciences*, *43*(23), 2886–2900.

Monin, A., & Yaglom, A. M. (2013). Statistical fluid mechanics volume II. Mechanics of Turbulence, Courier Corporation.

Morrison, H., Witte, M., Bryan, G. H., Harrington, J. Y., & Lebo, Z. J. (2018). Broadening of modeled cloud droplet spectra using bin microphysics in an eulerian spatial domain. *Journal of the Atmospheric Sciences*, *75*(11), 4005–4030.

Neggers, R., Duynkerke, P., & Rodts, S. (2003). Shallow cumulus convection: A validation of large-eddy simulation against aircraft and landsat observations. *Quarterly Journal of the Royal Meteorological Society*, *129*(593), 2671–2696.

Niedermeier, D., Chang, K., Cantrell, W., Chandrakar, K. K., Ciochetto, D., & Shaw, R. A. (2018). Observation of a link between energy dissipation rate and oscillation frequency of the large-scale circulation in dry and moist Rayleigh-Bénard turbulence. *Physical Review Fluids*, *3*(083), 501. https://doi.org/10.1103/PhysRevFluids.3.083501

Ovchinnikov, M., Ackerman, A. S., Avramov, A., Cheng, A., Fan, J., Fridlind, A. M., et al. (2014). Intercomparison of large-eddy simulations of arctic mixed-phase clouds: Importance of ice size distribution assumptions. *Journal of Advances in Modeling Earth Systems*, *6*, 223–248. https://doi.org/10.1002/2013MS000282

Ovchinnikov, M., & Easter, R. C. (2010). Modeling aerosol growth by aqueous chemistry in a nonprecipitating stratiform cloud. *Journal of Geophysical Research*, *115*, D14210. https://doi.org/10.1029/2009JD012816

Pedersen, J. G., Malinowski, S. P., & Grabowski, W. W. (2016). Resolution and domain-size sensitivity in implicit large-eddy simulation of the stratocumulus-topped boundary layer. *Journal of Advances in Modeling Earth Systems*, *8*, 885–903. https://doi.org/10.1002/2015MS000572

Pressel, K. G., Mishra, S., Schneider, T., Kaul, C. M., & Tan, Z. (2017). Numerics and subgrid-scale modeling in large eddy simulations of stratocumulus clouds. *Journal of advances in modeling earth systems*, *9*, 1342–1365. https://doi.org/10.1002/2016MS000778

Riechelmann, T., Noh, Y., & Raasch, S. (2012). A new method for large-eddy simulations of clouds with lagrangian droplets including the effects of turbulent collision. *New Journal of Physics*, *14*(6), 065008.

Shima, S.-i., Kusano, K., Kawano, A., Sugiyama, T., & Kawahara, S. (2009). The super-droplet method for the numerical simulation of clouds and precipitation: A particle-based and probabilistic microphysics model coupled with a non-hydrostatic model. *Quarterly Journal of the Royal Meteorological Society*, *135*(642), 1307–1320.

Siebert, H., & Shaw, R. A. (2017). Supersaturation fluctuations during the early stage of cumulus formation. *Journal of the Atmospheric Sciences*, *74*(4), 975–988.

Siebesma, A. P., Bretherton, C. S., Brown, A., Chlond, A., Cuxart, J., Duynkerke, P. G., et al. (2003). A large eddy simulation intercomparison study of shallow cumulus convection. *Journal of the Atmospheric Sciences*, *60*(10), 1201–1219.

Smolarkiewicz, P. K., & Grabowski, W. W. (1990). The multidimensional positive definite advection transport algorithm: Nonoscillatory option. *Journal of Computational Physics*, *86*(2), 355–375.

Sölch, I., & Kärcher, B. (2010). A large-eddy model for cirrus clouds with explicit aerosol and ice microphysics and lagrangian ice particle tracking. *Quarterly Journal of the Royal Meteorological Society*, *136*(653), 2074–2093.

Stevens, B., Cotton, W. R., Feingold, G., & Moeng, C.-H. (1998). Large-eddy simulations of strongly precipitating, shallow, stratocumulus-topped boundary layers. *Journal of the atmospheric sciences*, *55*(24), 3616–3638.

Stevens, B., & Lenschow, D. H. (2001). Observations, experiments, and large eddy simulation. *Bulletin of the American Meteorological Society*, *82*(2), 283–294.

Stevens, B., Moeng, C.-H., Ackerman, A. S., Bretherton, C. S., Chlond, A., de Roode, S., et al. (2005). Evaluation of large-eddy simulations via observations of nocturnal marine stratocumulus. *Monthly Weather Review*, *133*(6), 1443–1462.

Wyngaard, J. (1998a). Boundary-layer modeling: History, philosophy, and sociology.

Wyngaard, J. (1998b). Experiment, numerical modeling, numerical simulation, and their roles in the study of convection, *Buoyant convection in geophysical flows* (pp. 239–251). Dordrecht: Springer.

Xue, H., & Feingold, G. (2006). Large-eddy simulations of trade wind cumuli: Investigation of aerosol indirect effects. *Journal of the atmospheric sciences*, *63*(6), 1605–1622.

Yang, F., Kollias, P., Shaw, R. A., & Vogelmann, A. M. (2018). Cloud droplet size distribution broadening during diffusional growth: Ripening amplified by deactivation and reactivation. *Atmospheric Chemistry and Physics*, *18*(10), 7313–7328.